Lime application effects on soil aggregate properties: Use of the mean weight diameter and synchrotron-based X-ray µCT techniques

Talita R. Ferreira[a],[*], Luiz F. Pires[a],[*], Dorthe Wildenschild[b], André M. Brinatti[a], Jaqueline A.R. Borges[a], André C. Auler[a], Aline M.H. dos Reis[a]

[a] Laboratory of Physics Applied to Soils and Environmental Sciences, Department of Physics, State University of Ponta Grossa, Ponta Grossa, PR, Brazil
[b] School of Chemical, Biological, and Environmental Engineering, Oregon State University, Corvallis, OR, USA

ABSTRACT

The hierarchical organization of aggregates in soil is responsible for the presence of inter and intra-aggregate pores. This research aimed to investigate effects of soil surface liming, considering lime rates of 0, 10 and 15 t ha^{-1}, on the intra-aggregate porous system of soil aggregates with equivalent diameters of 2–4 and 1–2 mm, from 0 to 10 (A) and 10 to 20 cm (B) soil layers. These aggregates were selected by the wet sieving method carried out for determination of the mean weight diameter. Synchrotron-based computed microtomography (µCT) of aggregates was analyzed in terms of porosity, connectivity, tortuosity, and fractal dimension. Additionally, X-ray fluorescence was used to evaluate the elemental composition of the soil aggregates. All liming effects were concentrated at layer A, where calcium percentage was elevated in aggregates from 1–2 mm class as compared to those from 2–4 mm class. Accordingly, the physical parameters studied were generally more affected in the case of smaller aggregates (1–2 mm). Liming decreased total porosity, increased tortuosity of pores, and decreased fractal dimension for 1–2 mm aggregates, which was in line with the fact that larger pores were replaced by smaller ones in 1–2 mm aggregates, as found via both quantitative and qualitative analyses. On the other hand, liming did not affect pore connectivity under any of the circumstances.

1. Introduction

Soils that offer good structure for plant growth and adequate water storage and transport are characterized by the presence of stable aggregates (Hillel, 2004). These stable aggregates are responsible for the presence of inter and intra-aggregate pores inside the soil. Inter-aggregate pores, in turn, may respond differently from intra-aggregate pores to human and natural actions (Kutílek, 2004).

The mean weight diameter (MWD) is the most widely used index in relating aggregate size to stability (Nimmo and Perkins, 2002). Higher MWD indicates the dominance of less erodible, larger aggregates in the soil and, therefore, greater aggregate stability (Piccolo et al., 1997). However, this index does not offer any type of information about the porous space inside the aggregates. An important question is whether different aggregate sizes are associated with distinct soil pore space properties (e.g. porosity, connectivity and tortuosity of pores). Zhou et al. (2017), as an example, recently investigated effects of fertilizers on the bimodality of the soil pore structure by combining porosities of aggregates and core samples determined by computed microtomography. They observed differences only in the inter-aggregate

porosity, but not in the intra-aggregate porosity between the different sample sizes.

Individual aggregates are usually denser than a bulk sample (Dexter, 1988; Horn, 1990). Tiny soil aggregates are mainly characterized by the presence of intra-aggregate pores, which have great influence on the water hydrostatics and hydrodynamics (Tisdall and Oades, 1982; Kutílek et al., 2006). Therefore, the characterization of these pores is important from the environmental and physical points of view due to their relevance in other soil physical properties (Wang et al., 2012).

An important tool that can be used to evaluate the porous system of tiny soil aggregates is the X-ray computed microtomography (µCT). Synchrotron-based µCT is especially interesting given the spatial resolution achieved (Wildenschild et al., 2013). µCT has been used to investigate the influence of management systems in the soil structure, the long term vegetation restoration effect on soil aggregate structure and the organic matter distribution in terms of pore networks inside soil aggregates, to cite a few examples (Ngom et al., 2011; Zhou et al., 2012; Peth et al., 2014). Additionally, by applying concepts of mathematical morphology, geometrical characteristics of the intra-aggregate pore space such as its connectivity, elongation, tortuosity, lacunarity and

---

fractal dimension can be evaluated through μCT (Martínez et al., 2015; Tseng et al., 2018; Borges et al., 2018; Pires et al., 2017; Passoni et al., 2015; Chakraborti et al., 2003).

Liming is a soil treatment frequently used to reduce acidity problems, which reportedly affects soil structure, involving for example changes in soil biota and timing of the lime application (Holland et al., 2018). Liming was found to strengthen bonding related to water stability of aggregates (> 0.25 mm), which may be attributed to calcium (Ca) ion bridging between organic matter and clay mineral surfaces (Chan and Heenan, 1999). Ferreira et al. (2018a) showed that surface liming changed soil attenuation properties, for γ-ray radiation (59.5 keV and 661.6 keV), as influenced by the increase of Ca contents at the limed soil areas. In addition, there is evidence that aggregate formation, porosity and chemical properties are strongly related (Regelink et al., 2015) but, to this date, there are few scientific contributions concerning effects of soil amendments, including lime, specifically focusing on the intra-aggregate pore space (Zhou et al., 2013; Naveed et al., 2014; Wang et al., 2017).

The aim of this research was to identify the effects of soil surface liming (rates of 0, 10 and 15 t ha^{-1}) on the porous system of soil aggregates (diameters of 2–4 and 1–2 mm) by μCT. Analyses of porosity, connectivity, tortuosity, fractal dimension, and distributions of normalized porosity and number of pores as function of pore volume classes, were performed. Additionally, the mean weight diameter was determined to verify effects on soil aggregation, and XRF was used in an attempt to detect changes in elemental composition of soil aggregates.

2. Material and methods

The soil samples were collected from a rural site (25°28′S, 50°54′W, 821 m above sea level) located in the SE region of the Paraná State, Brazil. The soil was classified as Dystrudept silty-clay (Soil Survey Staff, 2013; Ferreira et al., 2018a, 2018b).

The study was established in May 2012 in a soil under no-till system (NTS). Lime rates of 0 (L0), 10 (L10), and 15 (L15) t ha^{-1} were applied on the surface without disturbing the soil. The lime used had 285 g kg^{-1} of CaO, 200 g kg^{-1} of MgO, 100.6% neutralizing power, 74.7% reactivity, and 75.1% total neutralizing relative power. Two soil layers, 0–10 cm (A) and 10–20 cm (B), were studied.

Effects of liming on chemical attributes of the soil under study were published elsewhere (Ferreira et al., 2018a) and are presented in Table 1 for a better understanding of the effects addressed here.

A total of 24 undisturbed monoliths (4 monoliths × 3 treatments × 2 layers) were manually collected (12 × 12 × 12 cm). The sample collection was carried out during the common bean (P. vulgaris L.) reproductive stage period (flowering), thirty months after the liming procedure. The reader is referred to Auler et al. (2017) for a more detailed description of the history of crop rotation adopted for the experiment under study.

The collected soil monoliths were manually disaggregated by carefully breaking them apart at their weakness planes. Then, the dis-aggregated soil monoliths were gently dry sieved through a 19 mm sieve, to homogenize the samples (Castro Filho et al., 2002; Briedis et al., 2012), and retained on an 8 mm sieve. Three portions of aggregates (100 g/portion) with diameters ranging from 8 to 19 mm, from each of the disaggregated monolith (totalizing 12 portions per treatment and layer), were selected (Fig. 1a) to be wet sieved.

The wet sieving was performed based on the process originally developed by Yoder (1936) and later adapted by Castro Filho et al. (1998). For this, a sequence of seven sieves was used, with mesh sizes of 8, 4, 2, 1, 0.5, 0.25, and 0.053 mm (Fig. 1b). The use of the 8 mm sieve in the wet sieving method is recommended for soils under NTS due to their capacity to form large stable aggregates (Madari et al., 2005; Tivet et al., 2013).

After the wet sieving, the set of aggregates retained in each sieve constituted the following classes: 8–19, 4–8, 2–4, 1–2, 0.5–1, 0.25–0.5, and 0.053–0.25 mm. The proportion of fragments > 0.25 mm constitutes the water-stable aggregates, whereas the 0.05–0.25 mm fraction represents the water-stable microaggregates (Dexter, 1988). In addition, the following classification was used in Tivet et al. (2013): macroaggregates (2–4 to 8–19 mm), mesoaggregates (0.25–0.5 to 1–2 mm) and microaggregates (0.053–0.25 mm), which applies to the present study. The aggregates from each class were dried at 40 °C in plastic containers. The mean weight diameter (MWD) was determined, for each portion (Fig. 1c), by using the equation presented in Hillel (2004), and the data distributions were displayed graphically using box plots.

Equal aliquots of aggregates from corresponding classes, among the four original monoliths of each treatment/layer, were selected and grouped; as a result, only one sample portion of aggregates for each class was formed for L0, L10, and L15 at soil layers A and B (Fig. 1d). Aggregate classes of 1–2, 0.5–1, 0.25–0.5 mm were mixed and the following classes were adopted for further analyses (to be described in the next paragraphs): 8–19 mm (c1), 4–8 mm (c2), 2–4 mm (c3), 0.25–2 mm (c4), and 0.053–0.25 mm (c5) (Fig. 1e).

For the X-ray fluorescence (XRF) measurements, equal portions of aggregates were taken from classes c1, c2, c3, c4, and c5, which were powdered and reduced to diameters lower than 45 μm (Fig. 2a,b). Approximately 2 g was placed into proper sample analysis cups covered with Mylar film (6 μm thickness) and a total of 30 samples was analyzed (5 classes × 3 treatments × 2 layers) (Fig. 2c). Three measurements were carried out for each sample using an energy dispersive XRF spectrometer model EDX-720 (Shimadzu), equipped with an Rh X-ray tube, in semi-quantitative mode. The voltage varied from 5 to 50 kV and its tube current from 1 to 1000 μA. The system detector was a Si(Li) semi-conductor cooled with liquid N at −196 °C. The measuring time for each sample was 100 s in Na-Sc (15 kV) and Ti-U (50 kV) energy bands. Measurements were performed under 30 Pa pressure and the spectral output was acquired in terms of elements. Standard procedures of calibration were performed whenever necessary (Pires et al., 2016).

For each soil treatment and layer, three water-stable aggregates

Table 1
Average chemical attribute (n = 4) results for 0–10 cm (layer A) and 10–20 cm (layer B) soil depths (Ferreira et al., 2018a).

	pH	OC	H + Al	Al^{3+}	Ca^{2+}	Mg^{2+}
		(g kg^{-1})	——————(cmol$_c$ dm^{-3})——————			
Layer A						
L0	3.93 (0.11)	36.50 (2.65)	15.35 (1.41)	4.15 (1.09)	1.53 (0.85)	2.55 (1.44)
L10	5.13 (0.43)	40.25 (7.59)	5.97 (2.04)	0.13 (0.15)	7.50 (2.16)	3.69 (2.45)
L15	5.59 (0.72)	42.00 (6.16)	4.31 (2.06)	0.10 (0.14)	8.95 (2.63)	4.63 (1.32)
Layer B						
L0	3.89 (0.09)	25.25 (2.06)	16.84 (1.29)	5.85 (1.29)	1.05 (0.61)	1.02 (0.54)
L10	4.01 (0.17)	23.50 (6.24)	15.42 (2.19)	5.28 (1.86)	1.61 (1.42)	1.53 (0.53)
L15	3.98 (0.09)	21.00 (1.63)	13.78 (3.80)	5.73 (0.67)	1.16 (0.43)	1.33 (0.17)

pH = in CaCl$_2$; OC = organic carbon content (Walkley-Black method); H + Al = potential acidity; Al^{3+}, Ca^{2+} and Mg^{2+} = exchangeable aluminum, calcium and magnesium; n = number of repetitions; values between parentheses represent the standard deviation.

SOIL TREATMENT: L0/L10/L15; SOIL LAYER: A/B

Monolith 1	Monolith 2	Monolith 3	Monolith 4

(a) Selection of aggregates

3 portions of aggregates of 8-19 mm	3 portions of aggregates of 8-19 mm	3 portions of aggregates of 8-19 mm	3 portions of aggregates of 8-19 mm

(b) Wet sieving

(c) Determination of MWD

Classes of aggregates per monolith:

8-19 mm	8-19 mm	8-19 mm
4-8 mm	4-8 mm	4-8 mm
2-4 mm	2-4 mm	2-4 mm
1-2 mm	1-2 mm	1-2 mm
0.5-1 mm	0.5-1 mm	0.5-1 mm
0.25-0.5 mm	0.25-0.5 mm	0.25-0.5 mm
0.053-0.25 mm	0.053-0.25 mm	0.053-0.25 mm
Portion 1	Portion 2	Portion 3

(d) Grouping of corresponding classes among the four monoliths

(e) Classes of aggregates adopted for further analyses

8-19 mm
4-8 mm
2-4 mm
1-2 mm
0.5-1 mm
0.25-0.5 mm
0.053-0.25 mm

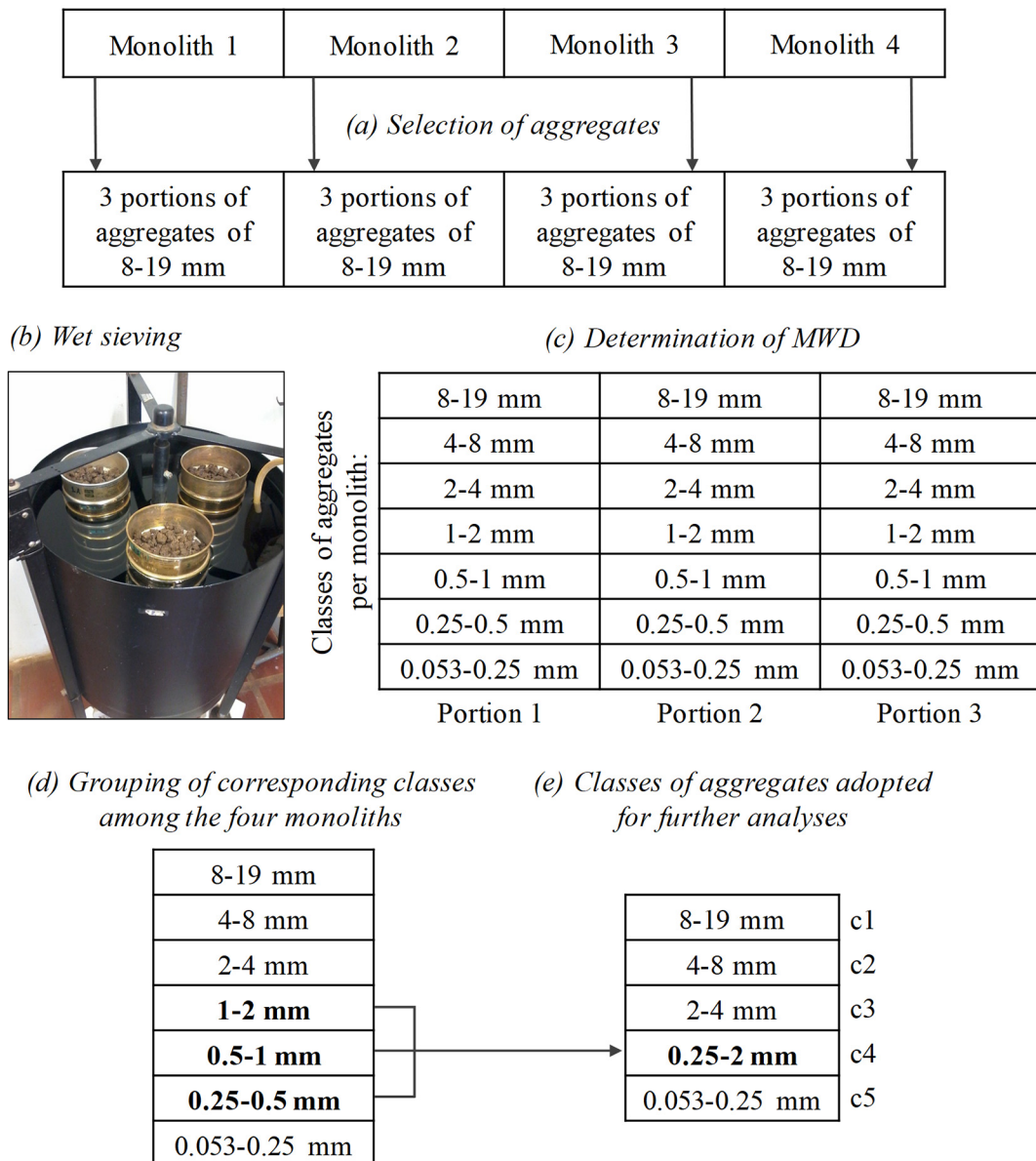|	
8-19 mm	c1
4-8 mm	c2
2-4 mm	c3
0.25-2 mm	c4
0.053-0.25 mm	c5

Fig. 1. Schematic representation of experimental procedures adopted for the separation of aggregates. Each portion contained 100 g of aggregates. Mesh sizes of 8, 4, 2, 1, 0.5, 0.25, and 0.053 mm were used for the wet sieving procedure. The mean weight diameter (MWD) was determined for each portion of each monolith and the mean value of this index, per soil treatment and layer, was calculated considering the 12 total number of portions in each case. Aggregates with diameters from 0.25 to 2 mm were mixed to generate five aggregate classes (c1, c2, c3, c4, and c5).
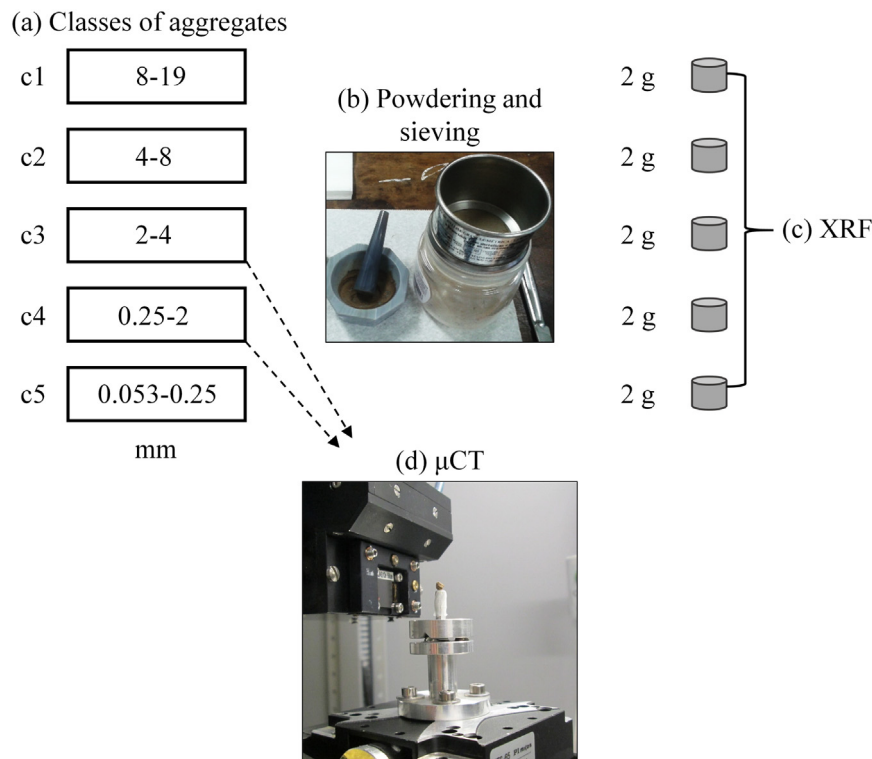
with diameters ranging from 2 to 4 mm (belonging to class c3 - macroaggregates) and from 1 to 2 mm (belonging to class c4 - mesoaggregates) were selected to be imaged in 3D (Fig. 2d). This selection was based on the field-of-view allowed by the μCT equipment.

Scanning was carried out at the Brazilian Synchrotron Light Source Facility (LNLS – CNPEM) at the IMX Beamline. Over an angle range of 180°, 1024 projections were acquired per sample, with a voxel size of 1.64 × 1.64 × 1.64 μm, pink beam, and 550 μm Silicon filter (around 50 min per sample). The detector was placed at a distance of 260 mm from the sample. A pco.2000 camera with sensor size of 2048 × 2048 pixels was used to image the scintillator, allowing a field-of-view of 3.4 × 3.4 mm for a 5× objective. The reconstruction procedure was carried out using in-house software, developed by the scientific computing group of LNLS (Miqueles et al., 2014). A conventional filtered-backprojection was used to reconstruct all three-dimensional datasets according to the backprojection formulation proposed in Miqueles et al. (2018).

The image visualization, processing, and analysis were performed using the commercial Avizo Fire™ software (v. 9.3). The raw data (I′) was denoised with a non-local means filter ($\hat{I}_{NL}$), search window: 15; local neighborhood: 3; similarity value: 1 (Buades et al., 2005). The gradient mask (20% standard deviation) was then applied ($\hat{I}_{NL+IG}$) to detect partial volume voxels at phase edges (Schlüter et al., 2014). The chosen search window parameter for the non-local means filter was evaluated based on the result of the image gradient mask. The adjustment of the local neighborhood parameter was a key step to reach a good result with the non-local means filter. If this value is either much smaller or much larger than fine structures in the data, the algorithm shows little or no effect (FEI, 2017).

The watershed segmentation algorithm was used to binarize the

(a) Classes of aggregates

c1	8-19
c2	4-8
c3	2-4
c4	0.25-2
c5	0.053-0.25

mm

(b) Powdering and sieving

2 g

2 g

2 g (c) XRF

2 g

2 g

(d) μCT

Fig. 2. (a) Classes of aggregates (c1, c2, c3, c4, and c5) that were (b) powdered and sieved for (c) X-ray Fluorescence (XRF) analysis; (d) selection of three aggregates from classes c3 and c4 for synchrotron-based X-ray μCT.

images (Vincent and Soille, 1991; Iassonov et al., 2009; Schlüter et al., 2014). Since there was no clear separation between the peaks of phases in the histogram, the threshold values were manually set, first capturing the air space as much as possible, without invading the solid phase, and then capturing the solid phase without bleeding into the air phase. The boundaries between phases were then delimited by the algorithm which additionally takes into account the detected phase edges, as it considers $\hat{I}_{NL+IG}$ as an input. The largest window of gray values left for the algorithm to resolve consisted of eight consecutive values (*e.g.* 132 and 140 being respectively the threshold values for the air and the solid phases).

The majority filter (kernel size: 3) was applied on the segmented images in order to prevent that isolated voxels or very small groups of voxels, with high probability of being associated with artifacts from the segmentation process, were considered as real pores (Peth et al., 2008; Katuwal et al., 2017).

The Avizo module *Volume Edit* was used to select the region of interest inside the μCT images for the subsequent analyses. The efficiency of the segmentation step, considering 2D slices from the selected region of interest, can be evaluated in Fig. 3. The largest possible volume was selected for each aggregate using a free-hand tool (draw + cut outside) and, in order to obtain the volume of that region (total volume of the sample, TVS), the Avizo module *Create Mask* was applied. The image based soil porosity (P, %) was evaluated by the ratio between the total volume of pores (TVP) - obtained with the Avizo module *Volume Fraction* - and the TVS: $P = TVP/TVS$ (Hillel, 2004).

The total number of pores (TNP), assumed as the total number of disconnected pores, as well as the volume of each isolated pore (VP), were obtained using a labeling algorithm in Avizo module *Label Analysis*. Values of TNP and VP were distributed in different pore volume classes: $0–10$; $10–10^2$; $10^2–10^3$; $10^3–10^4$; $10^4–10^5$; $10^5–10^9$ μm^3, for each sample. The resulting number of pores and volume of pores enclosed in each of these classes (NP_i and VP_i, respectively) were normalized by the TNP and TVP of each sample, respectively. In the last case, normalization of VP_i by TVP is equivalent as the normalization of

the porosity associated to each class ($P_i = VP_i/TVS$) by P. Therefore, the distribution of normalized P_i and NP_i as function of pore volume classes were displayed in graphics.

The connectivity and tortuosity of the porous space of each aggregate were characterized using Avizo modules *Euler 3D* and *Centroid Path Tortuosity*, respectively. The Euler number is an indicator of how connected a pore is to other pores: the smaller (more negative) the Euler number is, the better the pore connectivity (Wildenschild and Sheppard, 2013; Herring et al., 2013; Lehmann et al., 2006). A tortuosity number of one denotes a straight channel, while higher numbers indicate sinuous channels (Peth, 2010).

The Avizo module *Fractal Dimension 3D* was also employed to characterize the porous structure of the aggregates in terms of complexity. This module provides a number > 2 and strictly lower than 3, with numbers close to 2 representing standard geometric surfaces (Schmitt et al., 2016). When applied to 3D images, the fractal dimension is an effective indicator to measure and compare the roughness of a surface. In the case of segmented soil samples, the surface can be understood as the boundaries of the pores. The less smooth the surface is (which characterizes a more complex porous system), the higher the fractal dimension (FEI, 2017).

Differences between the three studied treatments (L0, L10, and L15), in each layer, were evaluated using a one-way ANOVA (considering results of MWD, P, Euler number, Tortuosity, and Fractal Dimension). If the ANOVA results were significant ($p < 0.5$), means were separated using a Tukey's studentized Range (HSD) test. For each treatment, the *t*-test (LSD) was used for comparisons between layers A and B. The Levene's test was performed to test for homogeneity of variances. All statistical analyses were performed using SAS software (University Edition; SAS Institute, Cary, NC, USA).

3. Results and discussion

From the distribution of MWD values shown in Fig. 4, it is noticed that all means are between 8 mm and 10 mm, which belongs to the
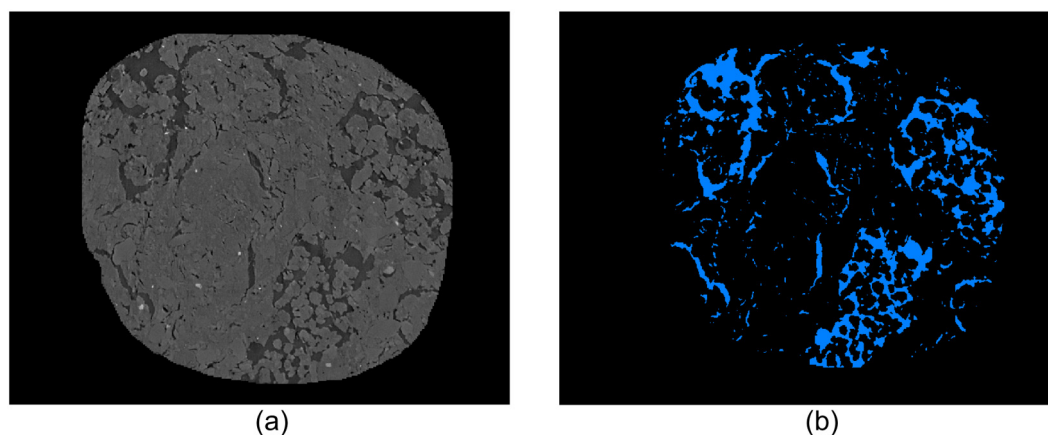
Fig. 3. 2D slices from the region of interest inside one of the 3D μCT images (a) in gray scale, after filtering step, where darker shades represent the air phase and brighter shades represent the solid phase; (b) after segmentation by the watershed method and application of the majority filter, where the blue color is labeled as the air phase. (For interpretation of the references to color in this figure legend, the reader is referred to the web version of this article.)

largest aggregate size class (c1). A few other studies have determined the MWD for soils under NTS, using a methodology similar to the one adopted here, and showed that NTS promotes indeed macroaggregation. For example, Madari et al. (2005) reported means of 7.9–5.4 mm, in different depths from 0 to 20 cm; Tivet et al. (2013) reported means in the range of approximately 11.0 to 9.0 mm, in different depths from 0 to 40 cm; and Briedis et al. (2012) found a mean of 10.3 mm in the 0–2.5 cm layer. Tivet et al. (2013) showed that the 8–19 mm aggregate size fraction, when compared to 4–8, 2–4, 1–2, and < 1 mm fractions, stocks 70% of the soil organic carbon (SOC), for a soil under NTS. According to the last mentioned authors, this illustrates the importance of large macroaggregates in protecting and stabilizing SOC.

In the case of Briedis et al. (2012), effects of lime treatments were evaluated in association with a long-term NTS experiment. These authors showed that a total lime rate of 9 t ha^{-1} (6 t ha^{-1} initially applied and 3 t ha^{-1} applied seven years later) increased the MWD from 10.3 mm to 11.4 mm over 15 years. In the present study, lime rates also increased the MWD at layer A, as seen from comparing L10 and L15 with L0 (Fig. 4a). Although L10 and L15 did not differ statistically, at layer A, it is possible to identify that the median tends to increase (Fig. 4a).

According to Briedis et al. (2012), the increase in MWD may be associated with the greater production of biomass and dry matter carbon input into the system due to liming. The closest attribute to infer on carbon in the present study is the measured content of organic carbon (OC) in the whole soil (Table 1). Although the content of OC in

the soil was not affected by liming, at neither of the soil layers, L15 presented a higher difference between OC contents from layers A and B, in comparison with L0 and L10. In corroboration, layers A and B are significantly different, for L15, regarding MWD (Fig. 4).

Detrimental effects of liming on the soil structure, such as aggregate breakdown and reduced infiltration rates, have been reported due to clay dispersion promoted by the initial increase of soil pH, when negative charges are increased and repulsive forces between particles are dominant (Roth and Pavan, 1991; Castro Filho and Logan, 1991). However, such detrimental effects generally occur in the first three months following lime applications and, after long periods, liming usually improves soil aggregation and aggregate stability (Haynes and Naidu, 1998; Bronick and Lal, 2005; Carmeis Filho et al., 2016; Chan and Heenan, 1998). This is related with the fact that pH also affects the concentrations of multi-valent cations, which reduces the repulsive force between particles and promotes flocculation (Haynes and Naidu, 1998).

Higher concentrations of exchangeable Ca, as seen in Table 1, increases aggregate formation since the interaction between organic matter and mineral particles depends on the concentration of exchangeable multi-valent cations (Regelink et al., 2015). According to Ghezzehei (2011), Ca and Mg promote formation of stable clay domains and, thus, their presence is crucial to the stability of soil structure.

At layer B (Fig. 4b), lime application did not present any effect on soil aggregation, which is in line with the lack of correction in soil acidity at this depth (Table 1).
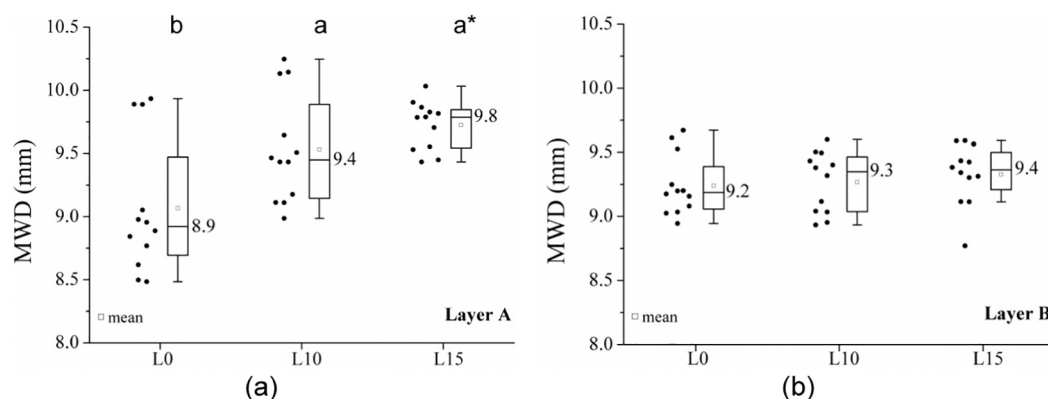
Fig. 4. Boxplot of mean weight diameter (MWD) (n = 12) of aggregates from a no-till soil without lime (L0) and under surface application of 10 (L10) and 15 (L15) t ha^{-1} lime rates, at soil layers (a) A (0–10 cm) and (b) B (10–20 cm). The horizontal line inside each box is the median. Data (•) outside of the range of the whiskers are regarded as outliers. Different letters represent significant differences between lime treatments within each layer (Tukey's HSD; p < 0.05) and asterisks represent significant differences between layers within each lime treatment (LSD t-test; p < 0.05).
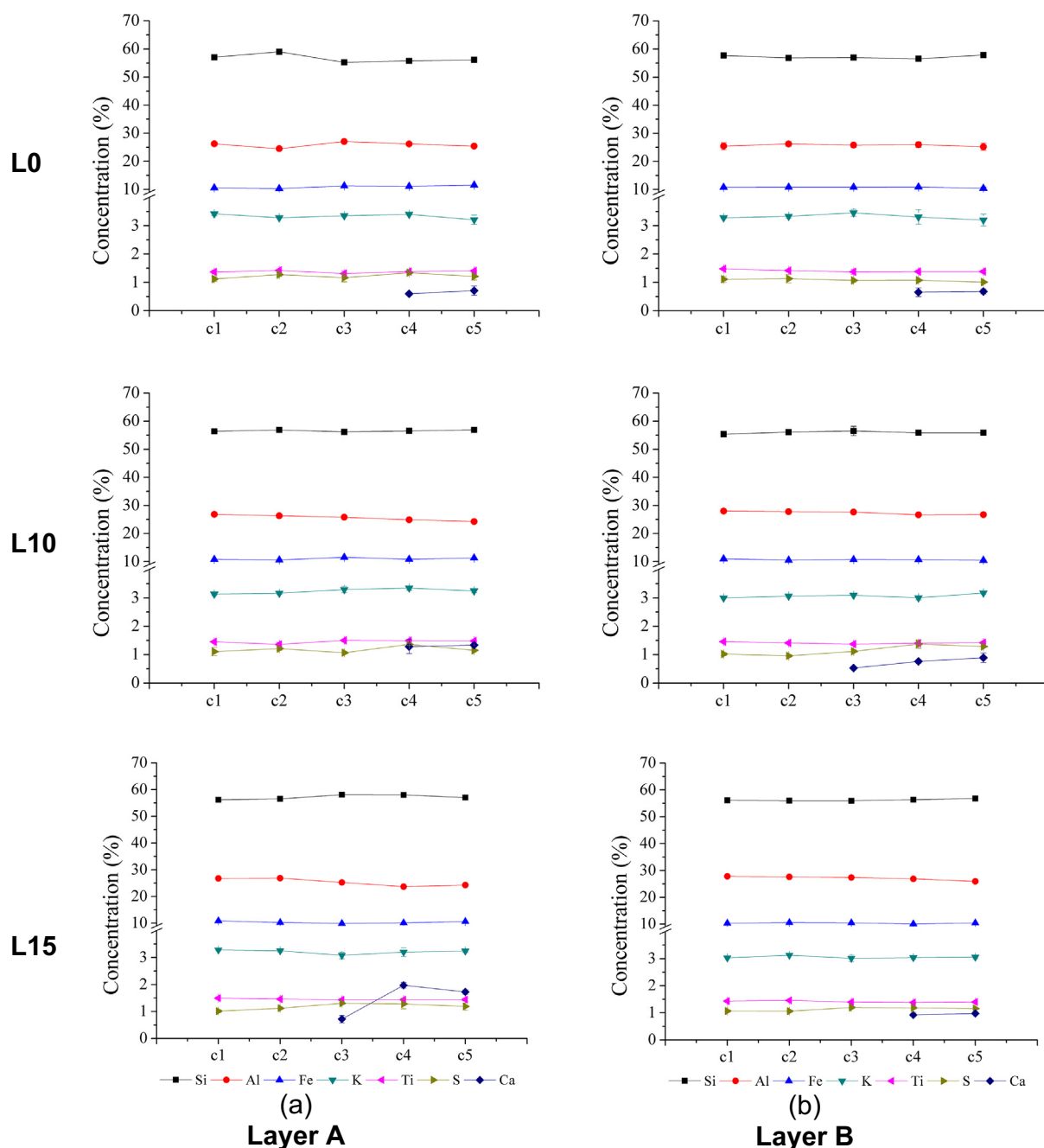
Fig. 5. Energy dispersive semi-quantitative XRF analysis of soil aggregates classified in the following size classes: 8–19 (c1), 4–8 (c2), 2–4 (c3), 0.25–2 (c4), and 0.053–0.25 (c5) mm at soil layers (a) A (0–10 cm) and (b) B (10–20 cm), from a no-till soil without lime (L0) and under surface application of 10 (L10) and 15 (L15) t ha^{-1} lime rates. Elements contributing with < 0.5% were disregarded. Vertical bars represent the standard deviation.

The semi-quantitative elemental characterization of soil aggregates classified in classes c1 – c5 (Fig. 2a), for layers A and B, is seen in Fig. 5. For all samples, Si, Al, and Fe are the major elements, followed by the contribution of minor ones (K, Ti, S, and Ca). The presence of Ca in smaller aggregates (c4 and c5 classes) for L0 - without lime application - at layer A and all treatments at layer B – where lime application (L10 and L15) was not efficient to improve soil chemical attributes (Table 1) – suggests that a small concentration of Ca is already inherent to the soil.

The elemental composition of soil aggregates shown in Fig. 5 agrees with the oxide composition of disturbed samples from the same soil under study here, as demonstrated in Ferreira et al. (2018a) by semi-quantitative XRF analyses. However, Ferreira et al. (2018a) have not

identified CaO in disturbed samples from L0 at layer A and in disturbed samples from neither of the treatments at layer B. This means that, in semi-quantitative XRF analyses, the low concentration of Ca present in small aggregates (Fig. 5) turns out to be insignificant in disturbed samples, in such a way that it does not reach the limit of the equipment detection. It should be mentioned that, instead of absolute concentration values, semi-quantitative XRF analysis provides the relative concentration (%) of each element in relation to the total.

From Fig. 5a, it is observed that the contribution of Ca progressively increases, at layer A, with lime rates. Specifically, in c4 and c5 classes, the amount of Ca increases from ~0.6% (L0) to ~1.3% for L10, and ~2% for L15. Although this variation is slight, it is relevant in comparison with the more stable contributions of the other elements among
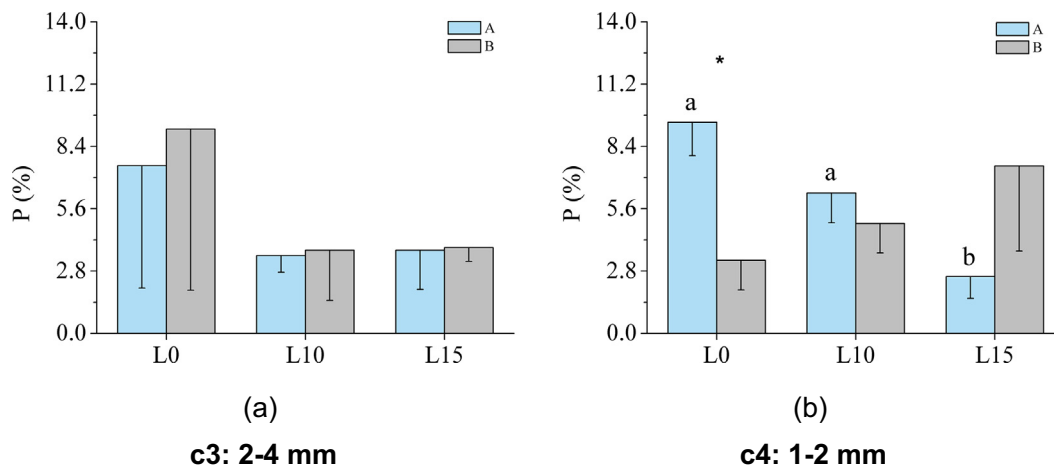
Fig. 6. Soil porosity (P) determined by μCT, from images with voxel size of 1.64 μm, for soil aggregates with diameter sizes of (a) c3: 2–4 mm and (b) c4: 1–2 mm, from a no-till soil without lime (L0) and under surface application of 10 (L10) and 15 (L15) t ha^{-1} lime rates, at soil layers A (0–10 cm) and B (10–20 cm). Vertical bars represent the standard deviation. Different letters represent significant differences between lime treatments within each layer (Tukey's HSD; $p < 0.05$) and asterisks represent significant differences between layers within each lime treatment (LSD *t*-test; $p < 0.05$).

soil treatments. Besides, Ca is identified in class c3 only for L15. It is important to mention that, if a different method of soil management was used, which could promote lime incorporation in depth, it is likely that amounts of Ca among soil aggregates at layer B would also be changed. This hypothesis is based on findings of Auler et al. (2017), who showed that lime has improved the soil chemical attributes at this depth with incorporation methods.

To this day, similar results were not reported in other studies and represent an important finding that can help explain processes related to soil aggregation as affected by liming. Because of that, the authors felt compelled to investigate whether higher amounts of Ca in smaller water-stable aggregates affect their porous space. The field-of-view allowed by the μCT equipment made it possible to scan aggregates exactly from the size classes of interest (c3: 2–4 mm and c4: 1–2 mm). It is important to mention that the selection of aggregates, which were subjected to aggregate stability tests, for μCT analyses was reported before (Rabbi et al., 2016). The μCT characterization of the intra-aggregate pore space in terms of porosity, number of pores, Euler number, tortuosity, and fractal dimension is presented in Figs. 6-9.

Lime treatments did not affect P in the case of larger aggregates (c3), at neither of the soil layers (Fig. 6a), even though a slight increase in contents of Ca for L15 in relation to L0 was observed at layer A for c3 (Fig. 5a). However, L15 promoted a reduction in P for smaller aggregates (c4), only at layer A (Fig. 6b). Considering that Ca is the only element that underwent relevant percentage changes in aggregates from c4 among treatments, at layer A (Fig. 5a), this may have collaborated to make the aggregates denser for L15 than for L0 and L10 (Fig. 6b).

The described reduction in P for c4 at layer A contrasts with most of the studies addressing effects of lime on the soil core-scale, which often report an increase in P due to this practice (Ferreira et al., 2018b; Haynes and Naidu, 1998; Auler et al., 2017). However, it must be taken into account that pore structure is highly different depending on the scale of analysis, *e.g.* soil-core and aggregate scales (Zhou et al., 2017). Only a few investigations have been made concerning liming effects on the pore system of soil aggregates, some of which show certain agreement with the results of the current research while some show opposite trends (Wang et al., 2017; Naveed et al., 2014).

When it comes to soil aggregates of different sizes, Wang et al. (2017) reported that the impact of lime treatment on size and morphology of macropores is higher for smaller aggregates because more cementitious compounds are expected in this case, leading to the decrease of the efficiency of airflow. In the same way, airflow is impaired

by a reduction in P due to liming in the case of c4 aggregates at layer A (Fig. 6b), but not in the case of c3 aggregates (Fig. 6a). On the other hand, Naveed et al. (2014) examined natural soil aggregates (8–16 mm diameter), using an industrial CT scanner with spatial resolution of 30 μm, from differently managed soils, one of them under lime application; it turned out that aggregates from the limed field were more porous than the ones from non-limed fields.

Because P did not vary at layer B for any of the aggregate size classes (Fig. 6), most likely due to the non-successful effect of liming at this depth (Table 1, Fig. 5b), the distribution of normalized P_i and NP_i as function of pore volume classes for each soil treatment is shown in Fig. 7 only for soil layer A. It can be noticed that the distribution of normalized NP_i did not vary among treatments considering both c3 and c4 classes (Fig. 7). In all cases, the higher normalized NP_i happens for pore volumes enclosed in the 10–100 μm^3 class.

Although the distribution of normalized P_i is also practically the same among treatments for c3 (Fig. 7a), an interesting variation is observed for c4 (Fig. 7b). In the latter case, it is noticed that the normalized P_i decreases from L0 to L15 in the highest class of pore volumes (10^5–10^9 μm^3), while the normalized P_i increases in lower classes. This means that with a lime rate of 15 t ha^{-1}, larger pores were replaced by smaller ones in c4 aggregates.

As a matter of fact, Fig. 8a,b show that in the case of c4 at layer A, L0 has a much more porous structure than L15, in agreement with Fig. 6b. The highest pore volume identified for L0 is clearly much larger than the highest pore volume identified for L15 (Fig. 8c,d), in agreement with the change in normalized P_i distribution (Fig. 7b). In addition, Fig. 8e,f show isolated pores (excluding the highest pore volume shown in Fig. 8c,d) from which a denser structure is visualized for L15 in comparison to L0. It is important highlighting that, for being less porous and consisting mainly of smaller pores, aggregates from L15 tend to hold water more strongly than aggregates from L0, when considering c4 class at layer A (Kutilek and Nielsen, 1994; Hillel, 2004).

From Fig. 9a,b, it is notable that connectivity has not changed with liming for neither of the aggregate size classes at none of the soil layers. This suggests that the lower contribution of more voluminous pores (10^5–10^9 μm^3) identified for L15 in comparison with L0 (Figs. 7b and 8c,d), in the case of aggregates from c4, was not relevant for the connectivity evaluation of the pore space as a whole. In addition, according to Lehmann et al. (2006), Euler number is negative for highly connected networks and positive for a set of isolated elements. Therefore, because of a high amount of small and isolated pores that constitutes the soil porous system of aggregates (Figs. 7 and 8e,f), the degree of
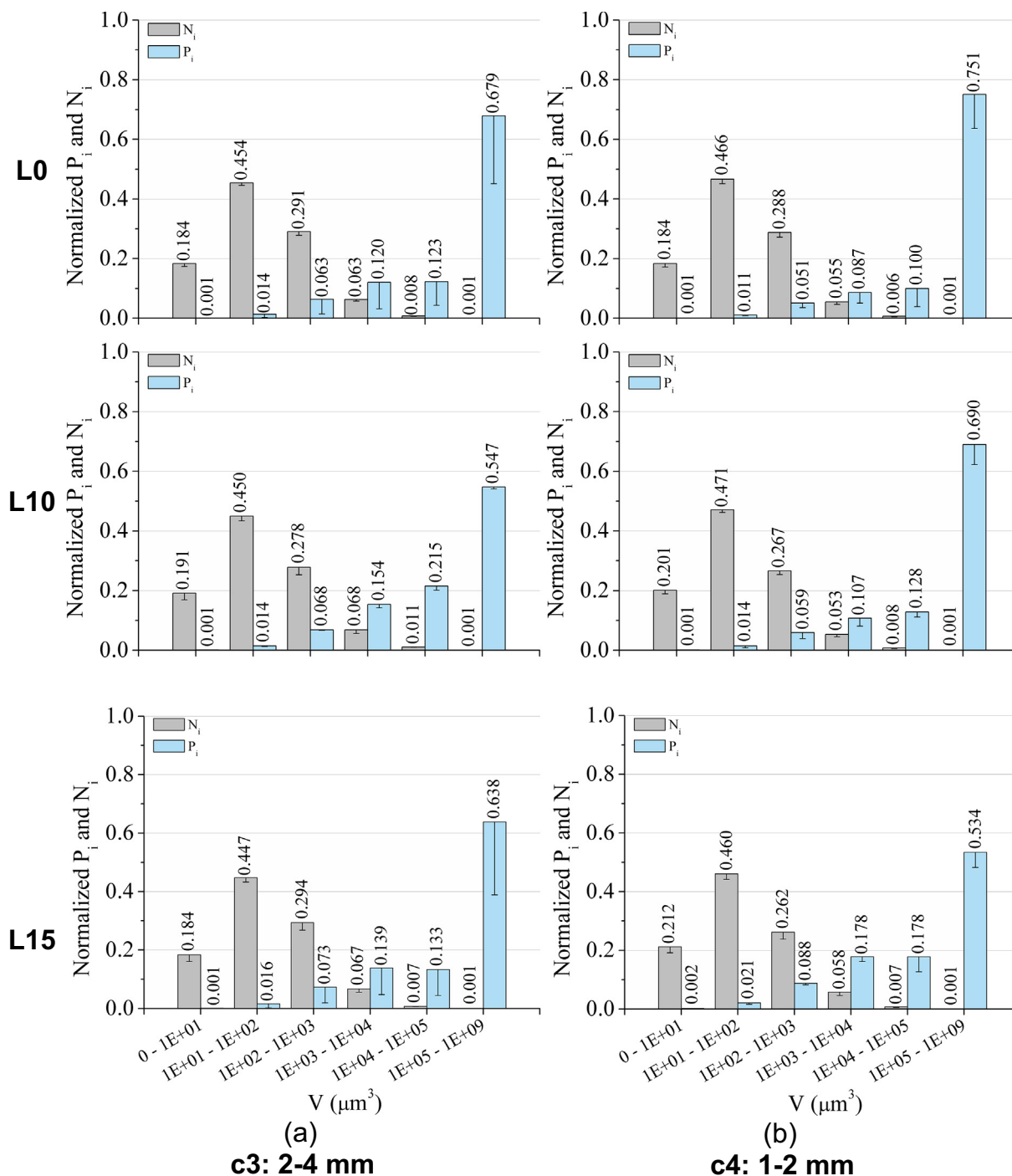
Fig. 7. Distribution of normalized P_i and NP_i as function of pore volume classes (0–10; 10–10^2; 10^2–10^3; 10^3–10^4; 10^4–10^5; 10^5–10^9 μm^3) for soil layer A (0–10 cm), considering soil aggregates with diameters of (a) c3: 2–4 mm and (b) c4: 1–2 mm from a no-till soil without lime (L0) and under surface application of 10 (L10) and 15 (L15) t ha^{-1} lime rates. P_i and NP_i, which represent the porosity and number of pores associated to the different pore volume classes, were normalized by soil porosity (P) and total number of pores (TNP), respectively. Vertical bars represent the standard deviation.

connectivity is low (positive values) in all cases (Fig. 9a,b).

Tortuosity has also not changed for class c3 at neither of the soil layers (Fig. 9c). However, tortuosity reached a maximum value for L15 in the case of aggregates from c4 at layer A (Fig. 9d). Therefore, in combination with the lower P and lower contribution of more voluminous pores (10^5–10^9 μm^3), identified in aggregates from c4 for L15 at layer A (Figs. 6b, 7b and 8c,d), the more tortuous aggregate pore space in the corresponding cases (Fig. 9d) is associated with a less favorable fluid transport through and into the intra-aggregate pore space. A similar relationship, regarding aggregates from different soil

management systems (conventionally tilled *vs.* grassland), is found in Peth et al. (2008). At layer B, tortuosity has not changed with liming in the case of aggregates from c4 (Fig. 5b).

Fig. 9f shows that fractal dimension decreased for L15 in comparison with L0 considering aggregates from c4 at layer A. The lower fractal dimension found for aggregates from L15 indicates that their pore structure became more homogeneous. A good representation of such enhanced homogeneity is seen in Fig. 8a,b, and, in addition, Fig. 10 shows that fractal dimension and P are indeed strongly related, as other studies have also demonstrated (Zhao et al., 2017; Dal Ferro

L0   L15
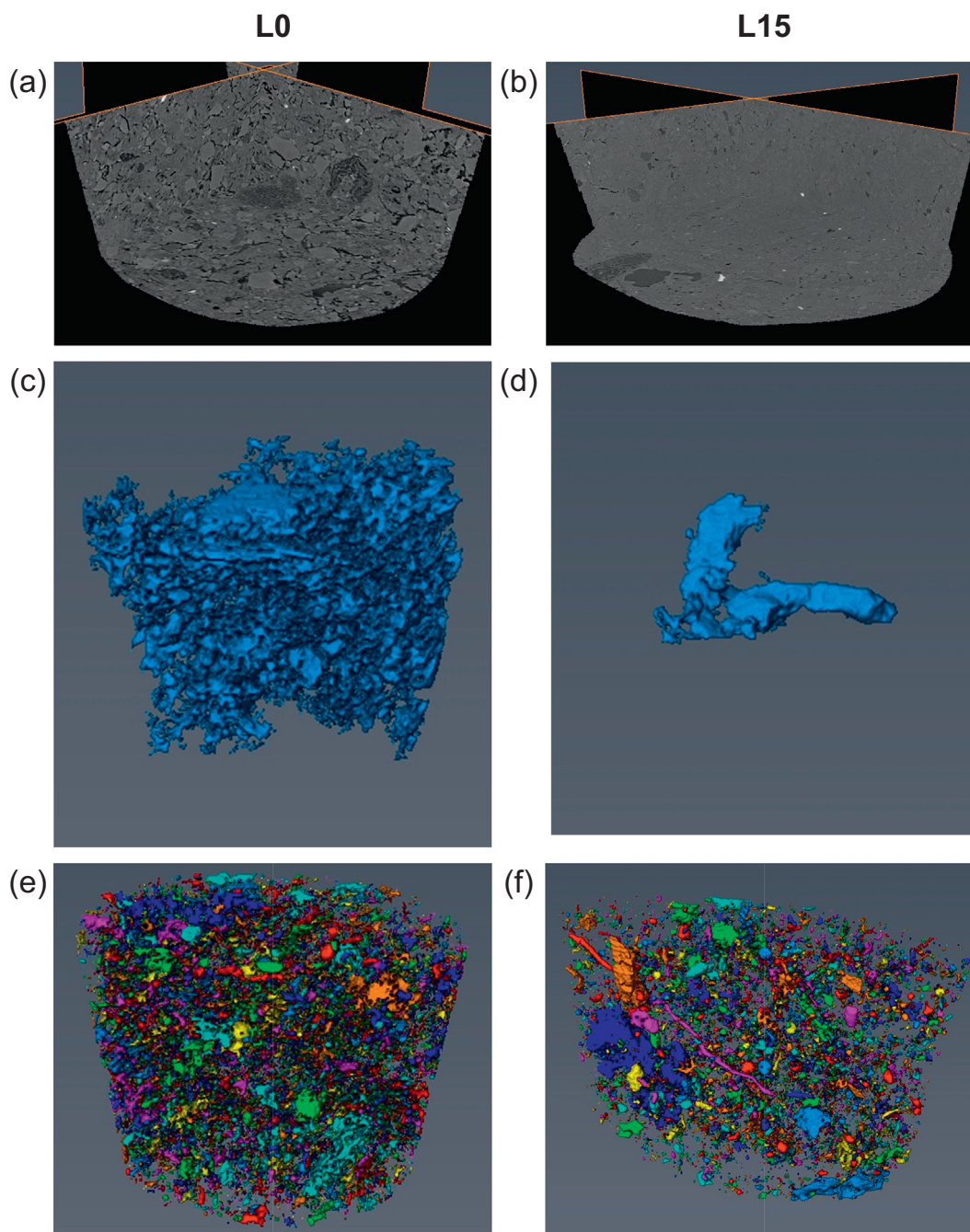
Fig. 8. (a,b) Cross sections, (c,d) most volumous pore and (e,f) porous space without the most volumous pore, with different colors representing isolated pores from the μCT images of 1–2 mm sized aggregates (c4) from L0 (no-till soil without lime) and L15 (no-till soil under surface application of 15 t ha^{-1} lime rate) treatments at soil layer A (0–10 cm).

et al., 2013). As previously described, in the case of c4 aggregates from L0, at layer A, P was found to consist of a higher proportion of more voluminous pores in comparison to L15 (Fig. 7b). The surfaces of those pores are naturally less smooth and consequently more complex than that of smaller and isolated pores.

From a general point of view, a smaller variability is often observed for c3 in comparison with c4 aggregates, considering results of P, connectivity, tortuosity, and fractal dimension. It should be mentioned that this might be related to the porosity exclusion principle (Dexter, 1988). According to this principle, each order of compound particles excludes the pore spaces between the particles of the next higher order, which explains the smaller standard deviation seen for the measured pore space properties of the smallest aggregates, allowing the

identification of nicer trends.

It is worth highlighting that, when working with irregular porous media, such as soil aggregates, a common difficulty is to delineate the boundaries of the media within μCT images, at the segmentation step, in order to separate it from the background (Wang et al., 2012). In brief, this may be accomplished by using a local thickness analysis, to obtain a rough outer surface, followed by morphological operations such as: closing, to close the smaller outer pores, and filling, to fill the largest internal voids, with post masking to preserve small features (Voltolini et al., 2017; Nunan et al., 2006). Delineating the aggregate would be the ideal way to investigate the intra-aggregate porous space because it would allow to account for the configuration of pores not only in the core region of the aggregate, as was done in the current research, but
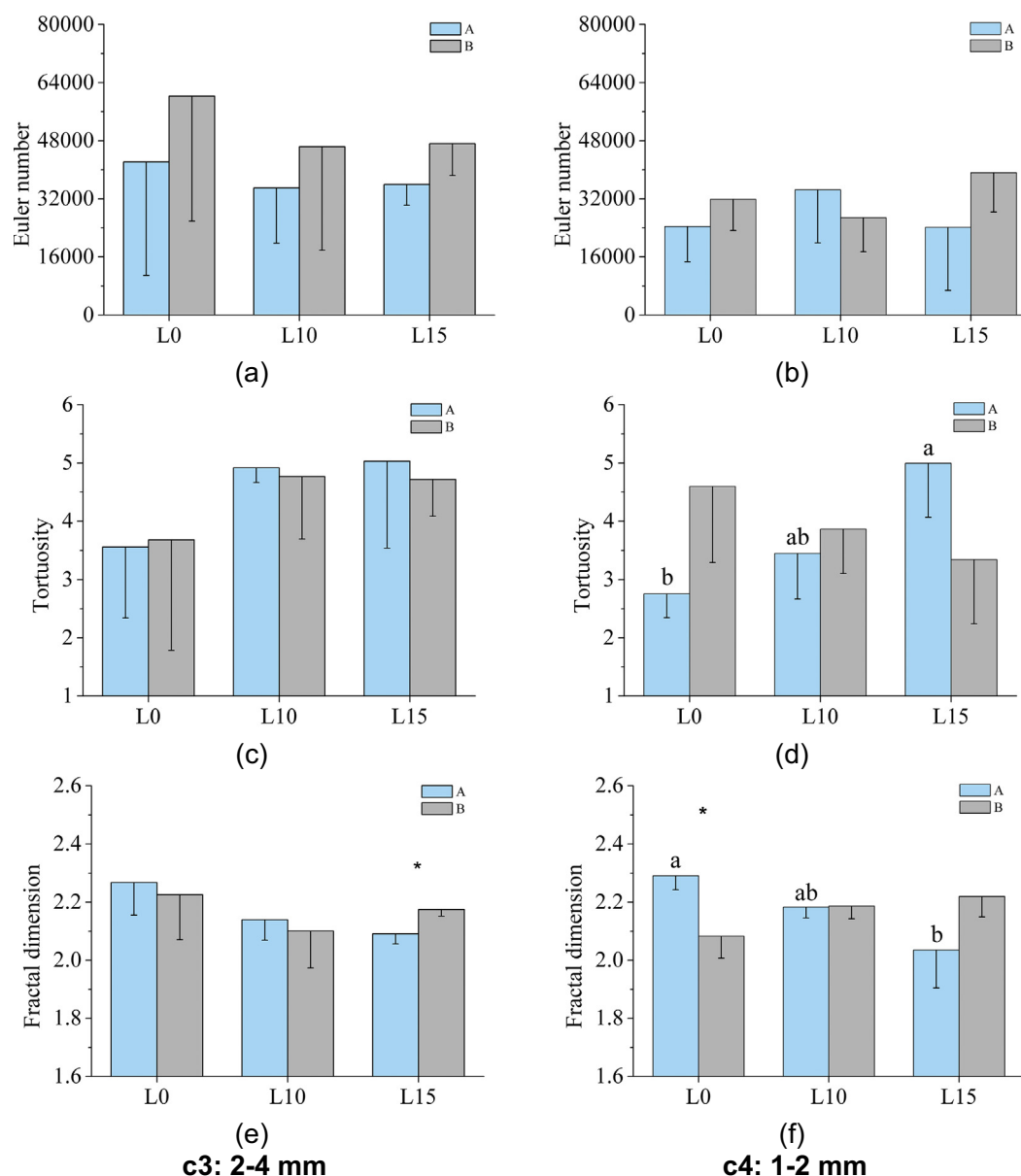
Fig. 9. Euler number, tortuosity and fractal dimension determined by μCT, from images with voxel size of 1.64 μm, for soil aggregates with diameter sizes of (a, c, e) c3: 2–4 mm and (b, d, f) c4: 1–2 mm, from a no-till soil without lime (L0) and under surface application of 10 (L10) and 15 (L15) t ha^{-1} lime rates, at soil layers A (0–10 cm) and B (10–20 cm). Vertical bars represent the standard deviation. Different letters represent significant differences between lime treatments within each layer (Tukey's HSD; p < 0.05) and asterisks represent significant differences between layers within each lime treatment (LSD t-test; p < 0.05).

also at its surface.

4. Conclusions

Surface liming improved soil aggregation by increasing the mean weight diameter at shallow depth, layer A (0–10 cm), but not deeper in the soil profile at layer B (10–20 cm). Calcium (Ca) was identified by XRF in aggregates selected from the wet sieving method with equivalent diameters ranging from 0.053 to 2 mm for all lime treatments (L0, L10, and L15) and both layers. However, the percentage of Ca in these aggregates progressively increased with the lime rates at layer A, where aggregates with equivalent diameter of 2–4 mm also turned out to show a low content of Ca in its elemental composition for L15.

The soil physical parameters analyzed by μCT images, considering aggregate sizes of 2–4 (c3) and 1–2 mm (c4), were in general more influenced by liming in the case of smaller aggregates. At shallow depth (layer A), liming was associated with a decrease in total porosity, an

increase in tortuosity of pores, and a decrease in fractal dimension for aggregates from c4. Such results suggest that, in aggregates from c4, liming has impaired the efficiency of air and water flow as well as has provided a more homogeneous intra-aggregate pore space. The last mentioned characteristic was corroborated by the fact that larger pores gave place to smaller ones in aggregates from c4, as quantitatively analyzed by the distribution of normalized porosity as function of pore volume classes and qualitatively by the visualization of the μCT images. Pore connectivity was not affected by liming at neither of the aggregate sizes and soil layers.
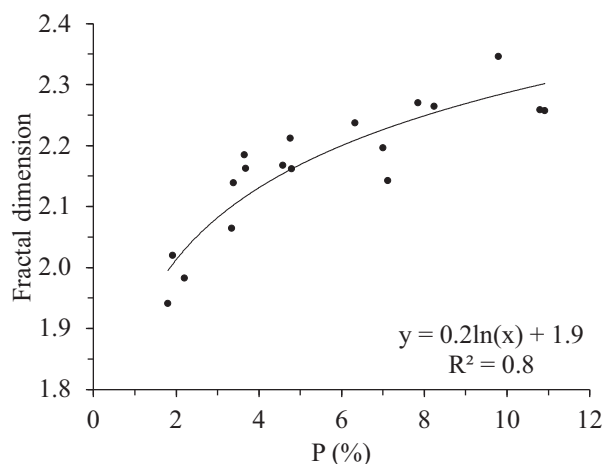
Acknowledgments

Fig. 10. Relationship between fractal dimension and porosity (P) of 1–2 mm sized aggregates (c4) from a no-till soil without lime (L0) and under surface application of 10 (L10) and 15 (L15) t ha^{-1} lime rates, at soil layer A (0–10 cm).

References

Auler, A.C., Pires, L.F., dos Santos, J.A.B., Caires, E.F., Borges, J.A.R., Giarola, N.F.B., 2017. Effects of surface-applied and soil-incorporated lime on some physical attributes of a Dystrudept soil. Soil Use Manag. 33, 129–140. https://doi.org/10.1111/sum.12330.

Borges, J.A.R., Pires, L.F., Cássaro, F.A.M., Roque, W.L., Heck, R.J., Rosa, J.A., Wolf, F.G., 2018. X-ray microtomography analysis of representative elementary volume (REV) of soil morphological and geometrical properties. Soil Tillage Res. 182, 112–122. https://doi.org/10.1016/j.still.2018.05.004.

Briedis, C., Sá, J.C. de M., Caires, E.F., Navarro, J. de F., Inagaki, T.M., Boer, A., Neto, C.Q., Ferreira, A. de O., Canalli, L.B., dos Santos, J.B., 2012. Soil organic matter pools and carbon-protection mechanisms in aggregate classes influenced by surface liming in a no-till system. Geoderma 170, 80–88. https://doi.org/10.1016/J.GEODERMA.2011.10.011.

Bronick, C.J., Lal, R., 2005. Soil structure and management: a review. Geoderma 124, 3–22. https://doi.org/10.1016/j.geoderma.2004.03.005.

Buades, A., Coll, B., Morel, J.M., 2005. A non-local algorithm for image denoising. In: Proceedings of the IEEE Computer Society Conference on Computer Vision and Pattern Recognition. IEEE Comput. Soc, San Diego, CA, pp. 60–65. https://doi.org/10.1109/CVPR.2005.38.

Carmeis Filho, A.C.A., Crusciol, C.A.C., Guimarães, T.M., Calonego, J.C., Mooney, S.J., 2016. Impact of amendments on the physical properties of soil under tropical long-term no till conditions. PLoS One 11, e0167564. https://doi.org/10.1371/journal.pone.0167564.

Castro Filho, C., Logan, T.J., 1991. Liming effects on the stability and erodibility of some Brazilian oxisols. Soil Sci. Soc. Am. J. 55, 1407. https://doi.org/10.2136/sssaj1991.03615995005500050034x.

Castro Filho, C., Muzilli, O., Podanoschi, A.L., 1998. Estabilidade dos agregados e sua relação com o teor de carbono orgânico num latossolo roxo distrófico, em função de sistemas de plantio, rotações de culturas e métodos de preparo das amostras. Soc. Bras. Ciênc. Solo 22, 527–538. https://doi.org/10.1590/S0100-06831998000300019.

Castro Filho, C., Lourenço, A., de F. Guimarães, M., Fonseca, I.C.B., 2002. Aggregate stability under different soil management systems in a red latosol in the state of Parana, Brazil. Soil Tillage Res. 65, 45–51. https://doi.org/10.1016/S0167-1987(01)00275-6.

Chakraborti, R.K., Gardner, K.H., Atkinson, J.F., Van Benschoten, J.E., 2003. Changes in fractal dimension during aggregation. Water Res. 37, 873–883. https://doi.org/10.1016/S0043-1354(02)00379-2.

Chan, K.Y., Heenan, D.P., 1998. Effect of lime (CaCO₃) application on soil structural stability of a red earth. Aust. J. Soil Res. 36, 73. https://doi.org/10.1071/S97054.

Chan, K.Y., Heenan, D.P., 1999. Lime-induced loss of soil organic carbon and effect on

aggregate stability. Soil Sci. Soc. Am. J. 63, 1841. https://doi.org/10.2136/sssaj1999.6361841x.

Dal Ferro, N., Charrier, P., Morari, F., 2013. Dual-scale micro-CT assessment of soil structure in a long-term fertilization experiment. Geoderma 204–205, 84–93. https://doi.org/10.1016/J.GEODERMA.2013.04.012.

Dexter, A.R., 1988. Advances in characterization of soil structure. Soil Tillage Res. 11, 199–238. https://doi.org/10.1016/0167-1987(88)90002-5.

FEI, 2017. Fractal Dimension Quantification and Non Local Means Filter Processing. http://developer97.openinventor.com/APIS/RefManJava/allclasses-noframe.html, Accessed date: 18 December 2017.

Ferreira, T.R., Pires, L.F., Brinatti, A.M., Auler, A.C., 2018a. Surface liming effects on soil radiation attenuation properties. J. Soils Sediments 18, 1641–1653. https://doi.org/10.1007/s11368-017-1866-2.

Ferreira, T.R., Pires, L.F., Wildenschild, D., Heck, R.J., Antonino, A.C.D., 2018b. X-ray microtomography analysis of lime application effects on soil porous system. Geoderma 324, 119–130. https://doi.org/10.1016/j.geoderma.2018.03.015.

Ghezzehei, T.A., 2011. Soil structure. In: Huang, P.M., Li, Y., Sumner, M.E. (Eds.), Handbook of Soil Sciences Properties and Processes - Part I: Soil Physics. CRC Press, Boca Raton, FL, USA, pp. 2.1–2.17.

Haynes, R.J., Naidu, R., 1998. Influence of lime, fertilizer and manure applications on soil organic matter content and soil physical conditions: a review. Nutr. Cycl. Agroecosyst. 51, 123–137. https://doi.org/10.1023/A:1009738307837.

Herring, A.L., Harper, E.J., Andersson, L., Sheppard, A., Bay, B.K., Wildenschild, D., 2013. Effect of fluid topology on residual nonwetting phase trapping: implications for geologic CO₂ sequestration. Adv. Water Resour. 62, 47–58. https://doi.org/10.1016/j.advwatres.2013.09.015.

Hillel, D., 2004. Soil structure and aggregation. In: Introduction to Environmental Soil Physics. Elsevier Academic Press, Burlington, Massachusetts, USA, pp. 73–89.

Holland, J.E., Bennett, A.E., Newton, A.C., White, P.J., McKenzie, B.M., George, T.S., Pakeman, R.J., Bailey, J.S., Fornara, D.A., Hayes, R.C., 2018. Liming impacts on soils, crops and biodiversity in the UK: a review. Sci. Total Environ. 610–611, 316–332. https://doi.org/10.1016/J.SCITOTENV.2017.08.020.

Horn, R., 1990. Aggregate characterization as compared to soil bulk properties. Soil Tillage Res. 17, 265–289. https://doi.org/10.1016/0167-1987(90)90041-B.

Iassonov, P., Gebrenegus, T., Tuller, M., 2009. Segmentation of X-ray computed tomography images of porous materials: a crucial step for characterization and quantitative analysis of pore structures. Water Resour. Res. 45. https://doi.org/10.1029/2009WR008087.

Katuwal, S., Hermansen, C., Knadel, M., Moldrup, P., Greve, M.H., de Jonge, L.W., 2017. Combining X-ray computed tomography and visible near-infrared spectroscopy for prediction of soil structural properties. Vadose Zo. J. 0, 0. https://doi.org/10.2136/vzj2016.06.0054.

Kutílek, M., 2004. Soil hydraulic properties as related to soil structure. Soil Tillage Res. 79, 175–184. https://doi.org/10.1016/j.still.2004.07.006.

Kutilek, M., Nielsen, D.R., 1994. Soil Hydrology. Catena Verlag, Cremlingen.

Kutílek, M., Jendele, L., Panayiotopoulos, K.P., 2006. The influence of uniaxial compression upon pore size distribution in bi-modal soils. Soil Tillage Res. 86, 27–37. https://doi.org/10.1016/j.still.2005.02.001.

Lehmann, P., Wyss, P., Flisch, A., Lehmann, E., Vontobel, P., Krafczyk, M., Kaestner, A., Beckmann, F., Gygi, A., Fluhler, H., 2006. Tomographical imaging and mathematical description of porous media used for the prediction of fluid distribution. Vadose Zo. J. 5, 80–97. https://doi.org/10.2136/vzj2004.0177.

Madari, B., Machado, P.L.O.A., Torres, E., de Andrade, A.G., Valencia, L.I.O., 2005. No tillage and crop rotation effects on soil aggregation and organic carbon in a Rhodic Ferralsol from southern Brazil. Soil Tillage Res. 80, 185–200. https://doi.org/10.1016/J.STILL.2004.03.006.

Martínez, F.S.J., Ortega, F.J.M., Monreal, F.J.C., Kravchenko, A.N., Wang, W., 2015. Soil aggregate geometry: measurements and morphology. Geoderma 237–238, 36–48. https://doi.org/10.1016/j.geoderma.2014.08.003.

Miqueles, E.X., Rinkel, J., O'Dowd, F., Bermúdez, J.S.V., 2014. Generalized Titarenko's algorithm for ring artefacts reduction. J. Synchrotron Radiat. 21, 1333–1346. https://doi.org/10.1107/S1600577514016919.

Miqueles, E., Koshev, N., Helou, E.S., 2018. A backprojection slice theorem for tomographic reconstruction. IEEE Trans. Image Process. 27, 894–906. https://doi.org/10.1109/TIP.2017.2766785.

Naveed, M., Arthur, E., de Jonge, L., Tuller, M., Moudrup, P., 2014. Pore structure of natural and regenerated soil aggregates: an X-ray computed tomography analysis. Soil Sci. Soc. Am. J. 78, 377–386.

Ngom, N.F., Garnier, P., Monga, O., Peth, S., 2011. Extraction of three-dimensional soil pore space from microtomography images using a geometrical approach. Geoderma 163, 127–134. https://doi.org/10.1016/J.GEODERMA.2011.04.013.

Nimmo, J.R., Perkins, K.S., 2002. Aggregate stability and size distribution. In: Dane, J.H., Topp, G.C. (Eds.), Methods of Soil Analysis. Part 4: Physical Methods. Soil Science Society of America, Madison, Wisconsin, pp. 317–328.

Nunan, N., Ritz, K., Rivers, M., Feeney, D.S., Young, I.M., 2006. Investigating microbial micro-habitat structure using X-ray computed tomography. Geoderma 133, 398–407. https://doi.org/10.1016/J.GEODERMA.2005.08.004.

Passoni, S., Pires, L.F., Heck, R., Rosa, J.A., 2015. Three dimensional characterization of soil macroporosity by X-ray microtomography. Soc. Bras. Ciênc. Solo 39, 448–457. https://doi.org/10.1590/01000683rbcs20140360.

Peth, S., 2010. Applications of microtomography in soils and sediments. In: Singh, B., Gräfe, M. (Eds.), Synchrotron-Based Techniques in Soils and Sediments. Elsevier, pp. 73–101. https://doi.org/10.1016/S0166-2481(10)34003-7.

Peth, S., Horn, R., Beckmann, F., Donath, T., Fischer, J., Smucker, A.J.M., 2008. Three-dimensional quantification of intra-aggregate pore-space features using synchrotron-radiation-based microtomography. Soil Sci. Soc. Am. J. 72, 897. https://doi.org/10.

2136/sssaj2007.0130.

Peth, S., Chenu, C., Leblond, N., Mordhorst, A., Garnier, P., Nunan, N., Pot, V., Ogurreck, M., Beckmann, F., 2014. Localization of soil organic matter in soil aggregates using synchrotron-based X-ray microtomography. Soil Biol. Biochem. 78, 189–194. https://doi.org/10.1016/j.soilbio.2014.07.024.

Piccolo, A., Pietramellara, G., Mbagwu, J.S.C., 1997. Use of humic substances as soil conditioners to increase aggregate stability. Geoderma 75, 267–277. https://doi.org/10.1016/S0016-7061(96)00092-4.

Pires, L.F., Brinatti, A.M., Prandel, L.V., da Costa Saab, S., 2016. Mineralogical composition of hardsetting soils and its effect on the radiation attenuation characteristics. J. Soils Sediments 16, 1059–1068. https://doi.org/10.1007/s11368-015-1318-9.

Pires, L., Borges, J., Rosa, J., Cooper, M., Heck, R., Passoni, S., Roque, W., 2017. Soil structure changes induced by tillage systems. Soil Tillage Res. 165, 66–79.

Rabbi, S.M.F., Daniel, H., Lockwood, P.V., Macdonald, C., Pereg, L., Tighe, M., Wilson, B.R., Young, I.M., 2016. Physical soil architectural traits are functionally linked to carbon decomposition and bacterial diversity. Sci. Rep. 6, 33012. https://doi.org/10.1038/srep33012.

Regelink, I.C., Stoof, C.R., Rousseva, S., Weng, L., Lair, G.J., Kram, P., Nikolaidis, N.P., Kercheva, M., Banwart, S., Comans, R.N.J., 2015. Linkages between aggregate formation, porosity and soil chemical properties. Geoderma 247–248, 24–37. https://doi.org/10.1016/J.GEODERMA.2015.01.022.

Roth, C.H., Pavan, M.A., 1991. Effects of lime and gypsum on clay dispersion and infiltration in samples of a Brazilian Oxisol. Geoderma 48, 351–361. https://doi.org/10.1016/0016-7061(91)90053-V.

Schlüter, S., Sheppard, A., Brown, K., Wildenschild, D., 2014. Image processing of multiphase images obtained via X-ray microtomography: a review. Water Resour. Res. 50, 3615–3639. https://doi.org/10.1002/2014WR015256.

Schmitt, M., Halisch, M., Fernandes, C.P., dos Santos, V.S.S., Weller, A., 2016. Fractal dimension: an indicator to characterize the microstructure of shale and tight gas sands considering distinct techniques and phenomena. In: International Symposium of the Society of Core Analysts. Society of Core Analysts, Snowmass, Colorado, USA, pp. 6.

Soil Survey Staff, 2013. Simplified Guide to Soil Taxonomy. USDA-Natural Resources Conservation Service, National Soil Survey Center, Lincoln, USA.

Tisdall, J.M., Oades, J.M., 1982. Organic matter and water-stable aggregates in soils. J. Soil Sci. 33, 141–163. https://doi.org/10.1111/j.1365-2389.1982.tb01755.x.

Tivet, F., de Moraes Sá, J.C., Lal, R., Briedis, C., Borszowskei, P.R., dos Santos, J.B., Farias, A., Eurich, G., Hartman, D. da C., Nadolny Junior, M., Bouzinac, S., Séguy, L., 2013. Aggregate C depletion by plowing and its restoration by diverse biomass-C inputs under no-till in sub-tropical and tropical regions of Brazil. Soil Tillage Res. 126, 203–218. https://doi.org/10.1016/J.STILL.2012.09.004.

Tseng, C.L., Alves, M.C., Crestana, S., 2018. Quantifying physical and structural soil properties using X-ray microtomography. Geoderma 318, 78–87. https://doi.org/10.1016/j.geoderma.2017.11.042.

Vincent, L., Soille, P., 1991. Watersheds in digital spaces: an efficient algorithm based on immersion simulations. IEEE Trans. Pattern Anal. Mach. Intell. 13, 583–598. https://doi.org/10.1109/34.87344.

Voltolini, M., Taş, N., Wang, S., Brodie, E.L., Ajo-Franklin, J.B., 2017. Quantitative characterization of soil micro-aggregates: new opportunities from sub-micron resolution synchrotron X-ray microtomography. Geoderma 305, 382–393. https://doi.org/10.1016/J.GEODERMA.2017.06.005.

Wang, W., Kravchenko, A.N., Smucker, A.J.M., Liang, W., Rivers, M.L., 2012. Intra-aggregate pore characteristics: X-ray computed microtomography analysis. Soil Sci. Soc. Am. J. 76, 1159. https://doi.org/10.2136/sssaj2011.0281.

Wang, Y., Cui, Y.-J., Tang, A.M., Benahmed, N., Duc, M., 2017. Effects of aggregate size on the compressibility and air permeability of lime-treated fine-grained soil. Eng. Geol. 228, 167–172. https://doi.org/10.1016/J.ENGGEO.2017.08.005.

Wildenschild, D., Sheppard, A.P., 2013. X-ray imaging and analysis techniques for quantifying pore-scale structure and processes in subsurface porous medium systems. Adv. Water Resour. 51, 217–246. https://doi.org/10.1016/j.advwatres.2012.07.018.

Wildenschild, D., Rivers, M.L., Porter, M.L., Iltis, G.C., Armstrong, R.T., Davit, Y., Anderson, S.H., Hopmans, J.W., 2013. Using synchrotron-based X-ray microtomography and functional contrast agents in environmental applications. In: Soil–Water–Root Processes: Advances in Tomography and Imaging. The Soil Science Society of America, Inc., pp. 1–22. https://doi.org/10.2136/sssaspecpub61.c1.

Yoder, R.E., 1936. A direct method of aggregate analysis of soils and a study of the physical nature of erosion losses. Agron. J. 28, 337. https://doi.org/10.2134/agronj1936.00021962002800050001x.

Zhao, D., Xu, M., Liu, G., Yao, X., Tuo, D., Zhang, R., Xiao, T., Peng, G., 2017. Quantification of soil aggregate microstructure on abandoned cropland during vegetative succession using synchrotron radiation-based micro-computed tomography. Soil Tillage Res. 165, 239–246. https://doi.org/10.1016/J.STILL.2016.08.007.

Zhou, H., Peng, X., Peth, S., Xiao, T.Q., 2012. Effects of vegetation restoration on soil aggregate microstructure quantified with synchrotron-based micro-computed tomography. Soil Tillage Res. 124, 17–23. https://doi.org/10.1016/J.STILL.2012.04.006.

Zhou, H., Peng, X., Perfect, E., Xiao, T., Peng, G., 2013. Effects of organic and inorganic fertilization on soil aggregation in an Ultisol as characterized by synchrotron based X-ray micro-computed tomography. Geoderma 195–196, 23–30. https://doi.org/10.1016/J.GEODERMA.2012.11.003.

Zhou, H., Mooney, S.J., Peng, X., 2017. Bimodal soil pore structure investigated by a combined soil water retention curve and X-ray computed tomography approach. Soil Sci. Soc. Am. J. 0, 0. https://doi.org/10.2136/sssaj2016.10.0338.